

Triggered massive and clustered star formation by combined H II regions G38.91-0.44 and G39.30-1.04

Jin-Long Xu,^{1,2} Jun-Jie Wang^{1,2} and Xiao-Lan Liu^{1,2,3}

¹ National Astronomical Observatories, Chinese Academy of Sciences, Beijing 100012, China
e-mail: xujl@bao.ac.cn

² NAOC-TU Joint Center for Astrophysics, Lhasa 850000, China

³ University of the Chinese Academy of Sciences, Beijing, 100080, China

Preprint online version: June 22, 2018

ABSTRACT

Aims. We investigate the triggered star formation occurring in the Infrared dark clouds (IRDC) G38.95-0.47 between H II regions G38.91-0.44 and G39.30-1.04, and study the detailed morphology, distribution, and physical parameters of the molecular gas and dust in this region.

Methods. We present the radio continuum, infrared, and CO molecular observations of infrared dark cloud (IRDC) G38.95-0.47 and its adjacent H II regions G38.91-0.44 (N74), G38.93-0.39 (N75), and G39.30-1.04. The Purple Mountain Observation (PMO) 13.7 m radio telescope was used to detect $^{12}\text{CO } J=1-0$, $^{13}\text{CO } J=1-0$ and $\text{C}^{18}\text{O } J=1-0$ lines. The carbon monoxide (CO) molecular observations can ensure the real association between the ionized gas and the neutral material observed nearby. To select young stellar objects (YSOs) associated this region, we used the GLIMPSE I catalog.

Results. The $^{13}\text{CO } J=1-0$ emission presents two large cloud clumps. The clump consistent with IRDC G38.95-0.47 shows a triangle-like shape, and has a steep integrated-intensity gradient toward H II regions G38.91-0.44 and G39.30-1.04, suggesting that the two H II regions have expanded into the IRDC. Four submillimeter continuum sources have been detected in the IRDC G38.95-0.47. Only the G038.95-00.47-M1 source with a mass of $117 M_{\odot}$ has outflow and infall motions, indicating a newly forming massive star. We detected a new collimated outflow in the clump compressed by G38.93-0.39. The derived ages of the three H II regions are 6.1×10^5 yr, 2.5×10^5 yr, and 9.0×10^5 yr, respectively. In the IRDC G38.95-0.47, the significant enhancement of several Class I YSOs indicates the presence of some recently formed stars. Comparing the ages of these H II regions with YSOs (Class I sources and massive G038.95-00.47-M1 source), we suggest that YSOs may be triggered by G38.91-0.44 and G39.30-1.04 together, which supports the radiatively driven implosion model. It may be the first time that the triggered star formation has occurred in the IRDC compressed by two H II regions. The new detected outflow may be driven by a star cluster.

Key words. Stars: formation — Stars: early-type — ISM: H II regions — ISM: individual objects (G38.91-0.44, G38.93-0.39, G38.95-0.47, G39.30-1.04)

1. Introduction

Massive stars play an important role in both the morphology and the chemical evolution of the interstellar medium (ISM), but their formation mechanism is still poorly understood. The formation of massive stars can be triggered by the action of H II regions. With the expansion of the H II regions, it may compress a pre-existing molecular cloud creating a compact clump, or sweep up the surrounding molecular material creating a dense molecular layer. The compact clump and dense molecular layer can be break apart and then may collapse to lead to the formation of new stars.

In the numerical study of star formation, the expanding H II regions can trigger star formation if the ambient molecular material is dense enough (Hosokawa & Inutsuka 2005; Dale et al. 2007). Collect and collapse (CC) and radiatively driven implosion (RDI) mechanisms may trigger star formation on the borders of H II regions (Elmegreen 1998). Several pieces of observational evidence have been found supporting these star formation mechanisms (e.g., Zavagno et al. 2007; Deharveng et al. 2008; Paron et al. 2009; Tibbs et al. 2012). Therefore, a detailed study of the star-forming regions at various wavebands is neces-

sary to trace the star formation scenario of H II region environments.

Infrared dark clouds (IRDCs) are considered potential cluster and massive star formation regions (Menten et al. 2005). In this paper, we present results of an IRDC G38.95-0.47 with a distance of ~ 2.9 kpc (Du & Yang 2008), located between H II regions G38.91-0.44 and G39.30-1.04. Because IR-dark clumps are absorption features against the mid-IR Galactic background emission, López-Sepulcre et al. (2010) suggested that IRDC G38.95-0.47 is most likely located at the near distance. Four millimeter continuum cores were detected in the IRDC G38.95-0.47 (Rathborne et al. 2006). Only the G038.95-00.47-M1 core has outflow and infall motions (López-Sepulcre et al. 2010). However, Alexander et al. (2013) did not detect the classical signposts of triggered star formation in this region and concluded that the triggered star formation has not occurred. The region G39.30-1.04 may be a newly identified H II region, while H II regions G38.91-0.44 and G38.93-0.39 are associated with the infrared bubbles N74 and N75, respectively (Churchwell et al. 2006; Deharveng et al. 2010; Sherman 2012).

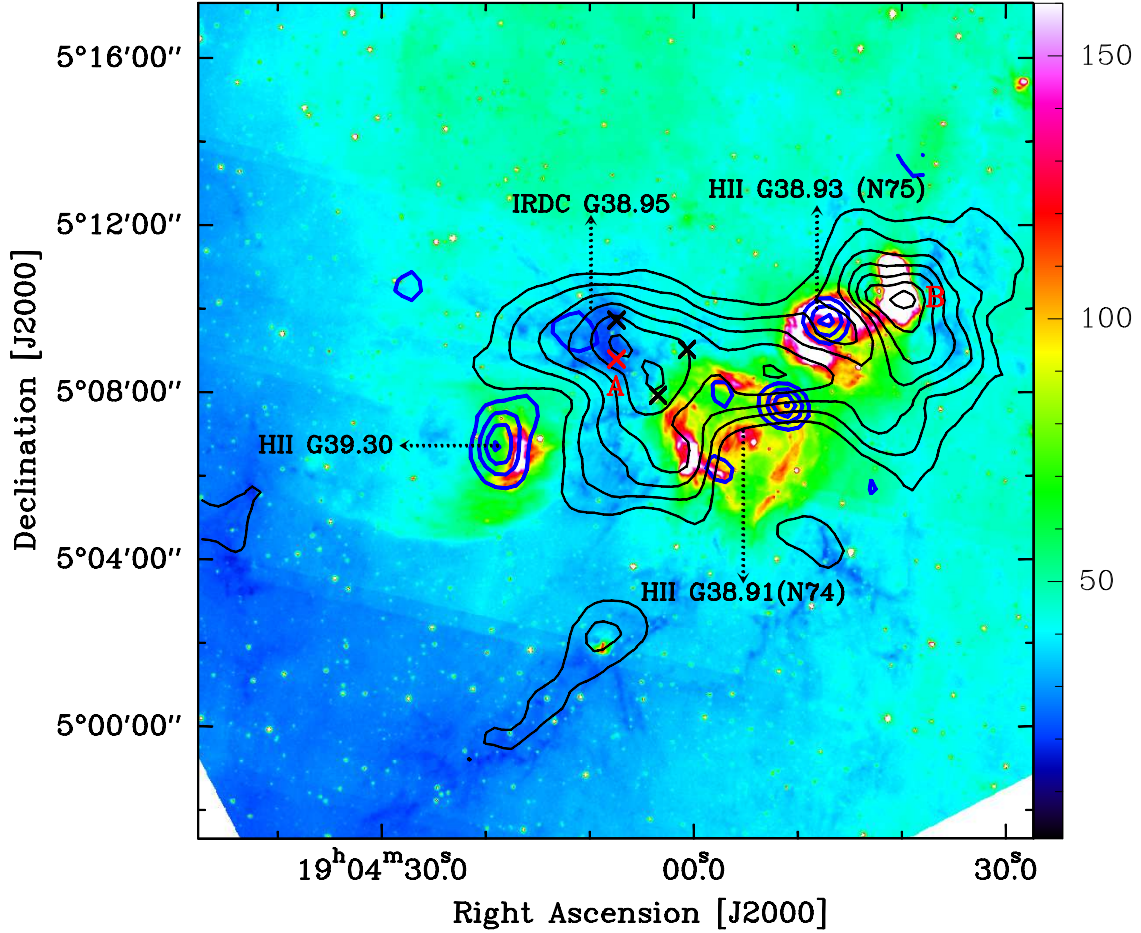


Fig. 1. $^{13}\text{CO } J=1-0$ integrated intensity contours (black) and 1.4 GHz radio continuum emission contours (blue) overlaid on the Spitzer-IRAC $8 \mu\text{m}$ emission map (color scale). The black contour levels are 30, 40, ..., 90% of the peak value (46.7 K km s^{-1}). The blue contour levels are 1.7, 3.3, 4.9, 6.5, and $8.1 \text{ mJy beam}^{-1}$. The letters A and B indicate the different cloud clumps. The green and red crosses indicate four millimeter continuum sources.

To look for signatures of star formation, we combined molecular, infrared, and radio continuum observations toward IRDC G38.95-0.47 and its adjacent H II regions.

2. Observations and data reduction

The mapping observations of IRDC G38.95-0.47 and its adjacent H II regions were performed in the $^{12}\text{CO } J=1-0$, $^{13}\text{CO } J=1-0$, and $\text{C}^{18}\text{O } J=1-0$ lines using the Purple Mountain Observation (PMO) 13.7 m radio telescope at De Ling Ha, China, in May 2012. The new 3×3 beam array receiver system in single-sideband (SSB) mode was used as front end. The back end is a fast Fourier transform spectrometer (FFTS) of 16384 channels with a bandwidth of 1 GHz, corresponding to a velocity resolution of 0.16 km s^{-1} for $^{12}\text{CO } J=1-0$ and 0.17 km s^{-1} for $^{13}\text{CO } J=1-0$ and $\text{C}^{18}\text{O } J=1-0$; $^{12}\text{CO } J=1-0$ was observed at upper sideband, while $^{13}\text{CO } J=1-0$ and $\text{C}^{18}\text{O } J=1-0$ were observed simultaneously at lower sideband. The half-power beam width (HPBW) was $53''$ at 115 GHz and the main beam efficiency was 0.5. The pointing accuracy of the telescope was better than $5''$. The system noise temperature (T_{sys}) in SSB mode varied between 150 K and 400 K. Mapping observations were centered at RA(J2000)= $19^{\text{h}}04^{\text{m}}07.5^{\text{s}}$, DEC(J2000)= $05^{\circ}08'18.9''$ using on-the-fly (OTF) observing mode. The total mapping area is $20' \times 20'$ in $^{12}\text{CO } J=1-0$, $^{13}\text{CO } J=1-0$, and $\text{C}^{18}\text{O } J=1-0$ with a $0.5' \times 0.5'$ grid. The standard chopper wheel calibration tech-

nique is used to measure antenna temperature T_{A}^* corrected for atmospheric absorption. The final data was recorded in brightness temperature scale of T_{mb} (K). The data were reduced using the GILDAS/CLASS¹ package. The 1.4 GHz radio continuum emission data were obtained from the NRAO VLA Sky Survey (Condon et al. 1998).

3. Results

3.1. Radio continuum and infrared emission of H II regions

Figure 1 shows the 1.4 GHz continuum emission image (blue contours) superimposed on the Spitzer-IRAC emission at $8 \mu\text{m}$ (color scale). The Spitzer-IRAC $8 \mu\text{m}$ emission is attributed to polycyclic aromatic hydrocarbons (PAHs), which can be used to trace the photodissociated region (PDR) surrounding H II region. In Fig. 1, the PAH emission displays a ring-like shape for the H II region G38.91-0.44, which coincides with bubble N74 (Churchwell et al. 2006; Deharveng et al. 2010; Sherman 2012). A small area of higher flux is situated at the center of the bubble, which could be a feature in the PDR on the far or near side of the bubble. Moreover, one compact and two weak radio continuum emissions (blue contours) are distributed along the PAH emission of G38.91-0.44. Anderson et al. (2011) determined that the hydrogen radio recombination line (RRL) velocity is 40

¹ <http://www.iram.fr/IRAMFR/GILDAS/>

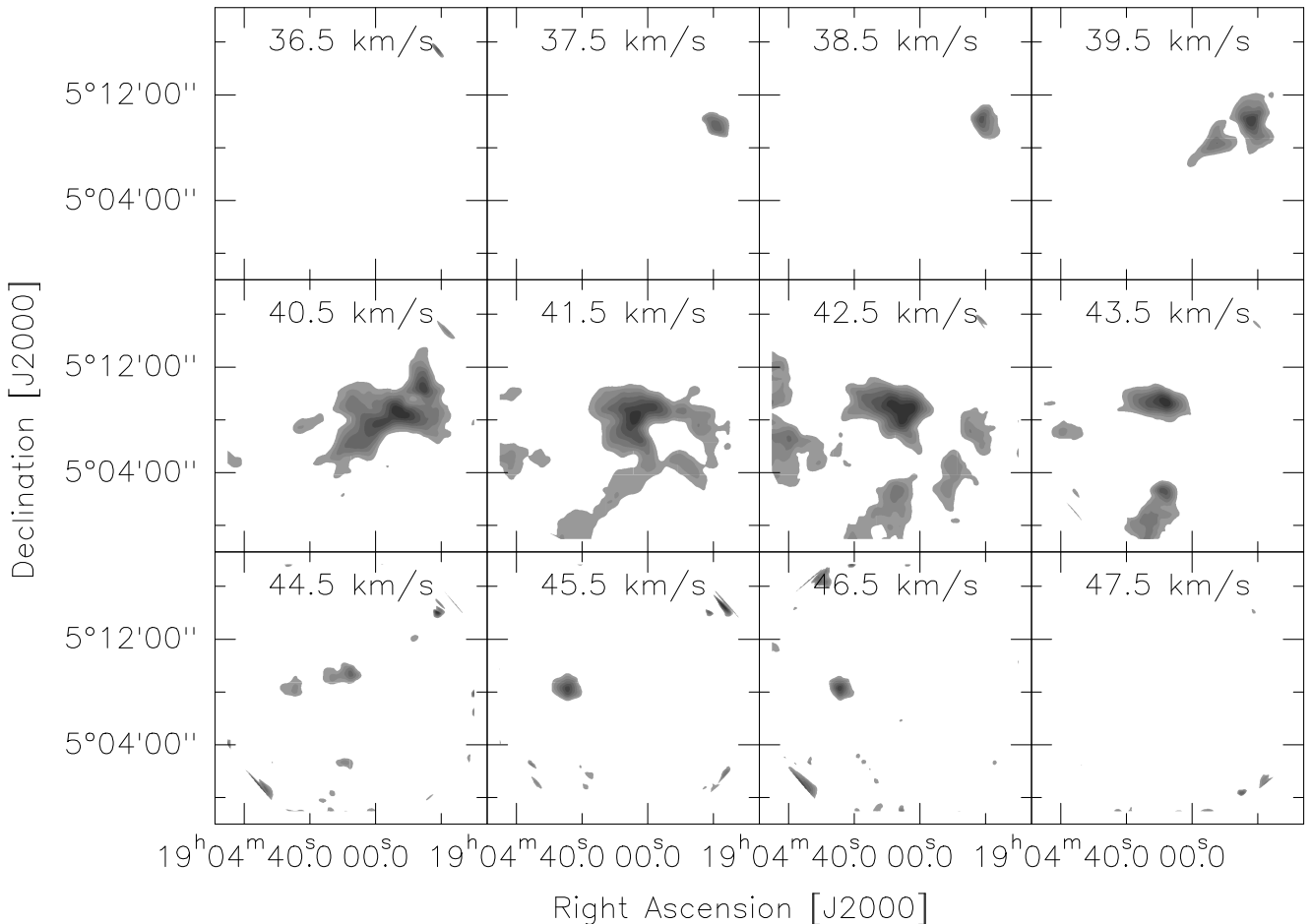


Fig. 2. $^{13}\text{CO } J=1-0$ channel maps each 1 km s^{-1} . Central velocities are indicated in each image.

km s^{-1} for G38.91-0.44. Hence, the triggered star formation is taking place in the molecular cloud at the periphery of PDR. There may be another new H II region to the east of G38.91-0.44, named G39.30-1.04 with $\text{RA(J2000)}=19^{\text{h}}04^{\text{m}}19.0^{\text{s}}$ and $\text{DEC(J2000)}=05^{\circ}06'42.7''$. The 1.4 GHz continuum emission reveals the presence of the ionized gas of G39.30-1.04. The PAH emission of G39.30-1.04 with a higher surface brightness shows a comet-like morphology. Because the ionized gas of G39.30-1.04 is surrounded by the PAH emission, the PAH emission may be excited by radiation from G39.30-1.04. The H II region G38.93-0.39 associated with bubble N75 (Churchwell et al. 2006; Deharveng et al. 2010; Sherman 2012) is located at the northwest of G38.91-0.44. From Fig. 1, we can see that the PAH emission of G38.93-0.39 show an almost semi-ring shape with a cut towards the southwest. The dense continuum emission is filled in the PAH emission of G38.93-0.39.

3.2. Molecular line emission

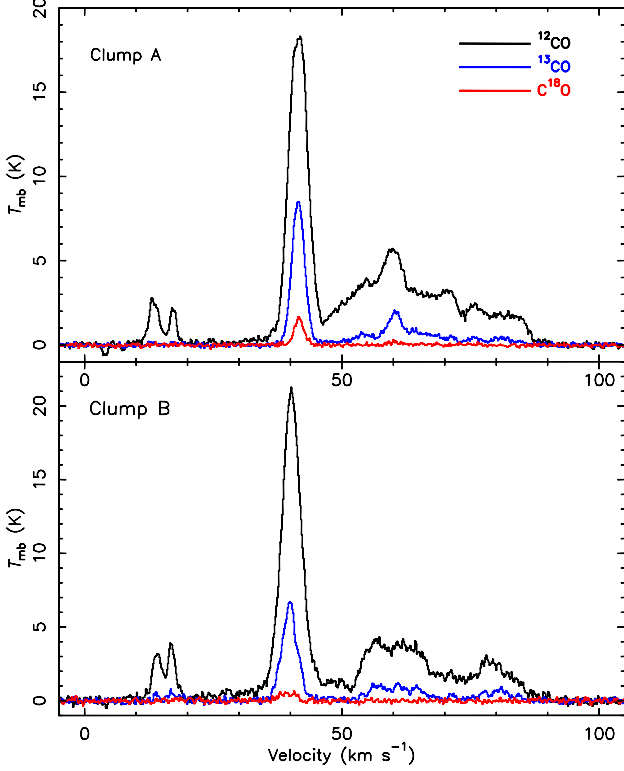
To analyze in greater detail the morphology of molecular gas associated with H II regions, we use the optically thin $^{13}\text{CO } J=1-0$ to trace the molecular gas. After a careful inspection of the CO component using the channel map (see Fig. 2), we find that only the CO component in intervals $37 \sim 47 \text{ km s}^{-1}$ is associated with these H II regions. Using this velocity range, we make the integrated intensity map of $^{13}\text{CO } J=1-0$ (Fig. 1). From Fig. 1 (black contours), we find two large cloud clumps, designated clumps A

and B, respectively. Clump A covers the whole IRDC G38.95-0.47, which is located between H II region G38.91-0.44 and G39.30-1.04. In addition, four submillimeter continuum sources were detected in the clump A (Di Francesco et al. 2008). Only G038.95-00.47-M1 core (marked by a red cross in figures 1 and 4) has outflow and infall motions (López-Sepulcre et al. 2010). Moreover, $^{13}\text{CO } J=1-0$ emission of clump A presents a triangle-like shape, and has an integrated intensity gradient along the direction of H II regions G38.91-0.44 and G39.30-1.04, suggesting that the shocks from the two H II regions have expanded into clump A, and have compressed it. Clump B shows a bow-like shape toward G38.93-0.39, the center of which has a small area of higher PAH emission. Mercer et al. (2005) detected a star cluster in clump B.

Figure 3 shows the average spectra of $^{12}\text{CO } J=1-0$, $^{13}\text{CO } J=1-0$, and $\text{C}^{18}\text{O } J=1-0$ over clumps A and B, respectively. From these spectra, we can see that the velocity components are mainly located in the velocity interval 30 to 50 km s^{-1} . The velocity component in interval 10 – 20 km s^{-1} should belong to the foreground emission, while 50 – 90 km s^{-1} may belong to the background emission, as seen in Fig. 2. We perform Gaussian fits to the spectra of $^{12}\text{CO } J=1-0$, $^{13}\text{CO } J=1-0$, and $\text{C}^{18}\text{O } J=1-0$ in clumps A and B. The fitted results are summarized in Table 1. Hence, we derive systemic velocities of $\sim 41.7 \text{ km s}^{-1}$ and $\sim 39.4 \text{ km s}^{-1}$ in the $\text{C}^{18}\text{O } J=1-0$ lines for clumps A and B, respectively, which are well associated with the hydrogen RRL velocity of H II region G38.91-0.44.

Table 1. Observed parameters of each line

Name	$^{12}\text{CO } J=1-0$			$^{13}\text{CO } J=1-0$			$\text{C}^{18}\text{O } J=1-0$		
	T_{mb} (K)	FWHM (km s $^{-1}$)	V_{LSR} (km s $^{-1}$)	T_{mb} (K)	FWHM (km s $^{-1}$)	V_{LSR} (km s $^{-1}$)	T_{mb} (K)	FWHM (km s $^{-1}$)	V_{LSR} (km s $^{-1}$)
Clump A	18.8	4.4 (0.2)	41.6 (0.1)	8.6	2.9(0.1)	41.5 (0.1)	1.6	2.2 (0.1)	41.7 (0.1)
Clump B	20.3	4.6 (0.2)	40.2 (0.1)	6.3	3.6(0.1)	38.9 (0.1)	0.5	3.7 (0.2)	39.4 (0.1)


Fig. 3. Average spectra of $^{12}\text{CO } J=1-0$, $^{13}\text{CO } J=1-0$, and $\text{C}^{18}\text{O } J=1-0$ over each clump.

Assuming local thermodynamical equilibrium (LTE) and using the optically thin $^{13}\text{CO } J=1-0$, the column densities of the clumps are determined by the Garden et al. (1991) equation

$$N_{^{13}\text{CO}} = 4.6 \times 10^{13} \frac{(T_{\text{ex}} + 0.89)}{\exp(-5.29/T_{\text{ex}})} \int T_{\text{mb}} dv \text{ cm}^{-2}, \quad (1)$$

where T_{ex} is the excitation temperature in K, and dv is the velocity range in km s $^{-1}$. We calculate T_{ex} following the equation $T_{\text{ex}} = 5.53/\ln[1 + 5.53/(T_{\text{mb}} + 0.82)]$, where T_{mb} is the corrected main-beam temperature of $^{12}\text{CO } J=1-0$. Here we use the relation $N_{\text{H}_2} \approx 5 \times 10^5 N_{^{13}\text{CO}}$ (Simon et al. 2001). If the clumps are approximately spherical in shape, the mean number density of H_2 is estimated to be $n(\text{H}_2) = 1.62 \times 10^{-19} N_{\text{H}_2}/d$, where d is the averaged diameter of the clumps in parsecs (pc). Moreover, their mass is given by $M_{\text{H}_2} = \frac{1}{6} \pi d^3 \mu_g m(\text{H}_2) n(\text{H}_2)$ (Garden et al. 1991), where $\mu_g = 1.36$ is the mean atomic weight of the gas, and $m(\text{H}_2)$ is the mass of a hydrogen molecule. The obtained column density, mean number density, and mass of each clump are all listed in Table 2.

3.3. Search for young stellar objects

To look for star formation toward IRDC G38.95-0.47 and its adjacent H II regions, we used the Spitzer-GLIMPSE I catalog.

Table 2. The physical parameters of the clumps in LTE.

Name	T_{ex} K	d pc	N_{H_2} (cm $^{-2}$)	$n(\text{H}_2)$ (cm $^{-3}$)	M ($10^5 M_{\odot}$)
Clump A	22.3	31.2	1.7×10^{22}	0.9×10^2	1.0
Clump B	23.7	34.8	1.6×10^{22}	0.8×10^2	1.1

The GLIMPSE I survey observed the Galactic plane ($65^\circ < |l| < 10^\circ$ for $|b| < 1^\circ$) with the four mid-IR bands (3.6, 4.5, 5.8, and 8.0 μm) of the Infrared Array Camera (Fazio et al. 2004). From the database, we extracted 9046 near-infrared sources within a circle of 10' in radius centered on R.A.=19^h04^m07.5^s (J2000), Dec=05^o08'18.9'' (J2000). Based on the color selection criteria of YSOs (Allen et al. 2004; Robitaille et al. 2008), we only selected the 103 Class I sources that had been detected in the four Spitzer-IRAC bands. Class I sources are protostars with circumstellar envelopes that are expected to be YSOs with an age of $\sim 10^5$ yr. Figure 4 presents the spatial distribution of Class I sources. From Fig. 4, we see that Class I sources are asymmetrically distributed across the whole selected region, and are mostly concentrated in IRDC G38.95-0.47 between H II regions G38.91-0.44 and G39.30-1.04. The existence of Class I sources may indicate star formation activity.

In addition, we found 13 *IRAS* sources using the *IRAS* Point Sources Catalog in this region. In Fig. 4, five *IRAS* sources may be associated with PAH emission. Because the fluxes of the five *IRAS* sources are only upper limits except for IRAS 19012+0505, we only calculate the parameters of IRAS 19012+0505. Infrared luminosity (Casoli et al. 1986) and dust temperature (Henning et al. 1990) are expressed respectively as,

$$L_{\text{IR}} = (6.196 \times F_{12} + 2.261 \times F_{25} + 1.373 \times F_{60} + 0.529 \times F_{100}) \times D^2, \quad (2)$$

$$T_{\text{d}} = \frac{96}{(3 + \beta) \ln(100/60) - \ln(F_{60}/F_{100})}, \quad (3)$$

where D is the distance from the sun in kpc, and F_{12} , F_{25} , F_{60} , and F_{100} are the infrared fluxes at four *IRAS* bands, 12 μm , 25 μm , 60 μm , and 100 μm , respectively. The emissivity index of dust particle (β) is assumed to be 2. In addition, we calculate the color index of each *IRAS* source. The calculated results are presented in Table 2.

4. DISCUSSION

The $^{13}\text{CO } J=1-0$ emission of IRDC G38.95-0.47 shows a triangle-like shape (see Figs. 1 and 4), and has a steep integrated-intensity gradient toward H II regions G38.91-0.44 and G39.30-1.04. We suggest that H II regions G38.91-0.44 and G39.30-1.04 have expanded into the IRDC G38.95-0.47. Four submillimeter continuum sources have been detected in the IRDC G38.95-0.47. Only source G038.95-00.47-M1 has outflow and infall motions, as well as a solar mass of 117 M_{\odot} , indicating that it is a newly forming massive star. Both kinetic timescales

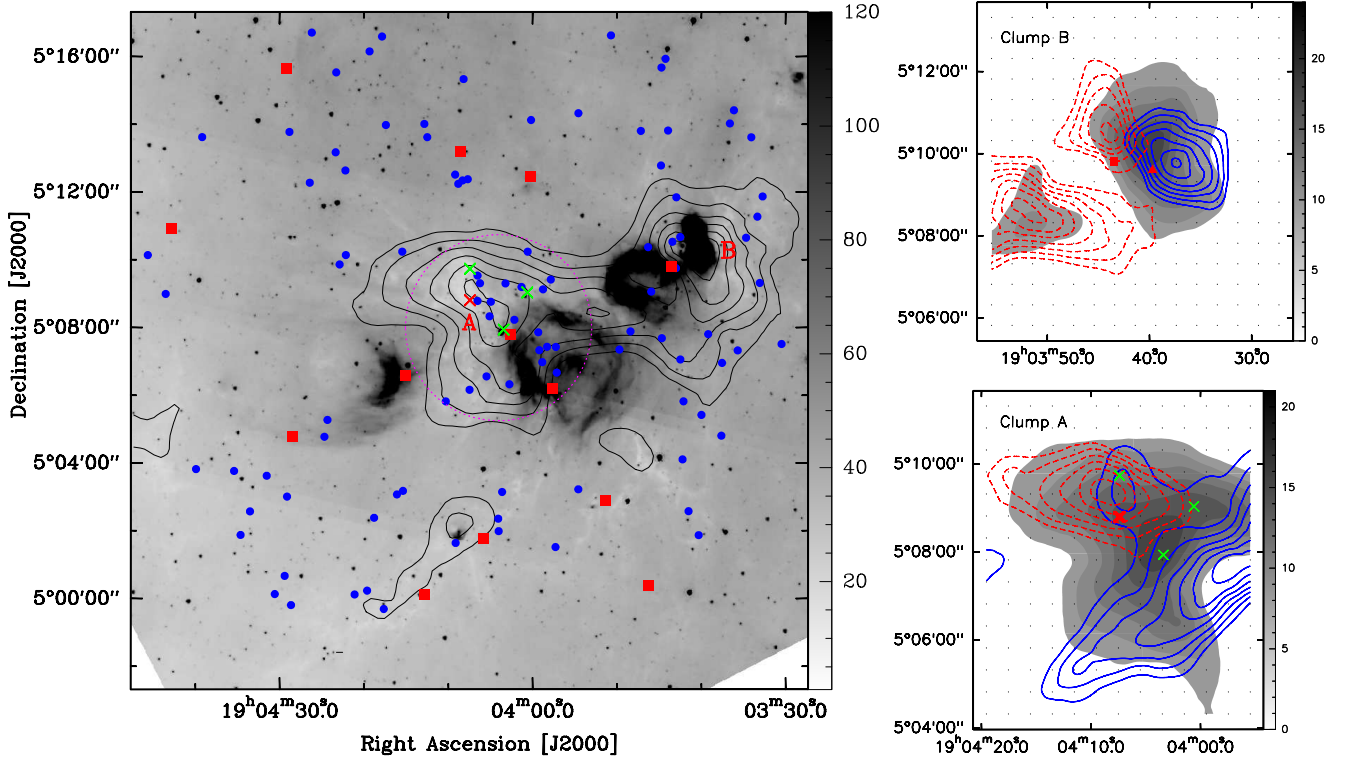


Fig. 4. Left: Class I sources are labeled as the blue dots. The red squares and triangle represent IRAS sources and Class II methanol maser (Deharveng et al. 2010), respectively. The green and red crosses indicate five 5mm continuum sources. The purple dashed circle outlines the Class I sources, which may be associated with IRDC G38.95-0.47. Right: the velocity-integrated intensity maps of $^{13}\text{CO } J = 1 - 0$ outflows (red and blue contours) overlaid with the $^{13}\text{CO } J = 1 - 0$ emission of each clump (gray scale). The red and blue contour levels are 30, ..., 100% of the peak value.

Table 3. Selected IR point sources associated with these H II regions: IR flux densities and the obtained parameters

Name	Source	RA (h m s)	DEC ($^{\circ}$ ' ")	F_{12} [Jy]	F_{25} [Jy]	F_{60} [Jy]	F_{100} [Jy]	$\log(\frac{F_{25}}{F_{12}})$	$\log(\frac{F_{60}}{F_{12}})$	L_{IR} [L_{\odot}]	T_{d} [K]
1	IRAS 19012+0505	19 03 43.51	05 09 48.91	8.27	17.31	497.20	1156.00	0.32	1.78	11644.14	91.62

of the outflow and infall are 4.7×10^4 yr (López-Sepulcre et al. 2010). Clump B shows a bow-like shape toward G38.93-0.39. We conclude that G38.93-0.39 has also expanded into clump B. Additionally, clump B is associated with a Class II methanol maser at 6.7 GHz (Deharveng et al. 2010). Class II methanol masers are considered signposts of recent massive star formation, but Zhang et al. (2005) did not detect the outflow in clump B coincident with IRAS 19012+0505. According to the color standard of Hughes & Macleod (1989), we find that IRAS 19012+0505 is associated with H II region G38.93-0.39. To confirm and explore the outflow motions in the two clumps, we show the distribution of the integrated intensity over the wings of the $^{13}\text{CO } J = 1 - 0$ profiles in Fig. 3 (right). We identify the wings with the velocity-position diagrams. In Fig. 3, we see that the $^{12}\text{CO } J = 1 - 0$ profiles are contaminated by the emission of the background source. The velocity component of blueshifted emission is from 39.7 km s^{-1} to 40.7 km s^{-1} , while the velocity component of redshifted emission is from 42.6 km s^{-1} to 43.6 km s^{-1} for G038.95-00.47-M1. In IRAS 19012+0505, the velocity component of blueshifted emission is from 36.5 km s^{-1} to 38.2 km s^{-1} , while the velocity component of redshifted emission is from 40.2 km s^{-1} to 41.0 km s^{-1} . In Fig. 4, the blueshifted and redshifted components are presented as

blue and red contours. From Fig. 4 (right), we clearly see that clump B has a collimated outflow activity at the NE-SW direction. Moreover, there is also outflow motion in clump A consistent with G038.95-00.47-M1. However, the blueshifted lobe of clump A is weak, which may be disrupted by the expansion of the H II region G38.91-0.44. Adopting the angle of 90° , the dynamic timescale of each outflow is estimated by equation $t = 9.78 \times 10^5 R/V$ (yr) (Goldsmith et al. 1984; Qin et al. 2008), where V in km s^{-1} is the maximum flow velocity relative to the cloud systemic velocity, and R in pc is the outflow size defined by the length of the begin-to-end flow extension for each blueshifted and redshifted lobe. Because IRDC G38.95-0.47 is associated with H II regions G38.91-0.44 and G39.30-1.04, we also adopt a kinematic distance of 2.9 kpc in this paper. The average dynamical timescale of the outflow in clump A is 2.8×10^5 yr, which is roughly consistent with the value in $\text{HCO}^+ J=1-0$ line (López-Sepulcre et al. 2010). For clump B, the outflow has the average dynamical timescale of 3.0×10^5 yr.

In addition, Class I sources are mostly concentrated in IRDC G38.95-0.47 between H II regions G38.91-0.44 and G39.30-1.04. Along the northeastern and eastern sides of N74 associated with G38.91-0.44, both Beaumont & Williams (2011) and Alexander et al. (2013) found a significant statistical overden-

sity of YSOs above the surrounding field. We do not know if all the selected sources seen in the direction of this region lie at the same distance as IRDC G38.95-0.47 relative to G38.91-0.44 and G39.30-1.04. However, the high density of YSOs located in the IRDC indicates that it is unlikely that they are all merely foreground and background stars. It is more likely that these YSOs are physically associated with IRDC G38.95-0.47, between H II regions G38.91-0.44 and G39.30-1.04.

The above analysis suggest that the triggered star formation have occurred in this region. The dynamical age of the H II region can also be used to decide whether YSOs are triggered by H II regions. Assuming an H II region expanding in a homogeneous medium, the dynamical age of the H II region can be estimated by the Dyson & Williams (1980) equation

$$t_{\text{HII}} = 7.2 \times 10^4 \left(\frac{R_{\text{HII}}}{\text{pc}} \right)^{4/3} \left(\frac{Q_{\text{Ly}}}{10^{49} \text{ph s}^{-1}} \right)^{-1/4} \left(\frac{n_i}{10^3 \text{cm}^{-3}} \right)^{-1/2} \text{ yr}, \quad (4)$$

where R_{HII} is the radius of the H II region, n_i is the initial number density of the gas, and Q_{Ly} is the ionizing luminosity. In previous studies toward several H II regions (e.g., Zavagno et al. 2006; Deharveng et al. 2008; Paron et al. 2009, 2011; Pomarès et al. 2009; Dirienzo et al. 2012), an initial number density of $\sim 10^3 \text{cm}^{-3}$ was determined. Alexander et al. (2013) gave the ionizing luminosity of $1.2 \times 10^{46} \text{ph s}^{-1}$, $2.1 \times 10^{46} \text{ph s}^{-1}$, and $6.6 \times 10^{45} \text{ph s}^{-1}$ for G38.91-0.44, G38.93-0.39 and G39.30-1.04, respectively. Adopting the measured radius of H II regions G38.91-0.44 ($\sim 1.4 \text{pc}$), G38.93-0.39 ($\sim 0.8 \text{pc}$), and G39.30-1.04 ($\sim 1.4 \text{pc}$) obtained from Fig. 1, and assuming an initial number density of $\sim 10^3 \text{cm}^{-3}$, we derived that the ages of these H II regions are $6.1 \times 10^5 \text{yr}$, $2.5 \times 10^5 \text{yr}$, and $9.0 \times 10^5 \text{yr}$, respectively. Comparing the ages of these H II regions with YSOs (Class I sources and massive G038.95-00.47-M1 source), we suggest that the YSOs located in IRDC G38.95-0.47 are likely to be triggered by G38.91-0.44 and G39.30-1.04 together. Deharveng et al. (2003) suggest that some dense fragments are regularly spaced along the H II region, providing strong evidence in favor of the CC model. In this picture, the shock fronts of G38.91-0.44 and G39.30-1.04 have driven into clump A, and have compressed some pre-existing cores in the IRDC G38.95-0.47. Furthermore, the PAH emission of G39.30-1.04 shows the cometary globule, supporting the RDI model. It may be the first time that the triggered massive and clustered stars formation has occurred in the IRDC compressed by two H II regions. We detected an outflow in clump B. Because the age of G38.93-0.39 is slightly smaller than that of the outflow, we conclude that the triggered star formation has not occurred in clump B, as we also did not find a significant statistical overdensity of YSOs (10^5yr) surrounding G38.93-0.39. Clump B is consistent with a star cluster (Mercer et al. 2005), hence the outflow may be driven by the cluster.

5. Conclusions

We have shown the $^{12}\text{CO } J = 2 - 1$, $^{12}\text{CO } J = 3 - 2$, and $^{13}\text{CO } J = 2 - 1$ molecular, infrared, and radio continuum observations towards IRDC G38.95-0.47 and its adjacent H II regions G38.91-0.44 (N74), G38.93-0.39 (N75), and G39.30-1.04. The results can be summarized as follows:

1. The $^{13}\text{CO } J=1-0$ emission shows two large cloud clumps. The clump associated with IRDC G38.95-0.47 shows a triangle-like shape, and has a steep integrated-intensity gradient toward H II regions G38.91-0.44 and G39.30-1.04, indicating that the two H II regions have expanded into the IRDC.

2. Four submillimeter continuum sources have been detected in the IRDC G38.95-0.47. Only the G038.95-00.47-M1 source has outflow and infall motions. In addition, the selected young stellar objects (YSOs) (Class I sources) are concentrated in the IRDC G38.95-0.47, which appear to be sites of ongoing star formation. The obtained ages of the three H II regions are $6.1 \times 10^5 \text{yr}$, $2.5 \times 10^5 \text{yr}$, and $9.0 \times 10^5 \text{yr}$. Taking into account the age of H II regions and YSOs (Class I sources and massive G038.95-00.47-M1 source), we suggest that YSOs may be triggered by the combined energy G38.91-0.44 and G39.30-1.04, supporting the radiatively driven implosion model. It may be the first time that the triggered star formation has occurred in the IRDC compressed by two H II regions.
3. We detected a new collimated outflow in the clump compressed by G38.93-0.39. The new detected outflow may be driven by a star cluster.

Acknowledgements. We are very grateful to the anonymous referee for his/her helpful comments and suggestions. We are also grateful to the staff at the Qinghai Station of PMO for their assistance during the observations. Thanks for the Key Laboratory for Radio Astronomy, CAS, for partly supporting the telescope operation. This work was supported by the National Natural Science Foundation of China (Grant No. 11363004).

References

- Alexander, M. J., Koblunicky, H. A., Kerton, C. R., & Arvidsson, K. 2013, *ApJ*, 770, 1
- Allen, L. E., Calvet, N., D'Alessio, P., 2004, *ApJS*, 154, 363
- Anderson, L. D., Bania, T. M., Balsa, D. S., & Rood, R. T. 2011, *ApJ*, 194, 32
- Beaumont, C. N. & Williams, J. P. 2011, *ApJ*, 709, 791
- Condon, J. J., Cotton, W. D., Greisen, E. W., et al., 1998, *AJ*, 115, 1693
- Casoli, F., Combes, F., Dupraz, C., Gerin, M., & Boulanger, F., 1986, *A&A*, 169, 281
- Churchwell, E., Povich, M. S., Allen, D., et al. 2006, *ApJ*, 649, 759
- Dale, J. E., Bonnel, I. A., Whitworth, A. P. 2007, *MNRAS*, 375, 1291
- Deharveng, L., Lefloch, B., Zavagno, A., et al. 2003, *A&A*, 408, L25
- Deharveng, L., Lefloch, B., Kurtz, S., et al. 2008, *A&A*, 482, 585
- Deharveng, L., Schuller, F., Anderson, L. D., et al. 2010, *A&A*, 523, 6
- Dirienzo, W. J., Indebetouw, R., Brogan, C. 2012, *ApJ*, 144, 173
- Dyson, J. E., & Williams, D. A. 1980, *Physics of the interstellar medium*, ed. Dyson, J. E. & Williams, D. A.
- Du, F., & Yang, J. 2008, *ApJ*, 686, 384
- Elmegreen, B. G. 1998, in *Origins*, ed. C. E. Woodward, J. M. Shull, & H. A. Thronson, *ASP Conf. Ser.*, 148, 150
- Fazio, G. G., Hora, J. L., Allen, L. E., et al. 2004, *ApJS*, 154, 10
- Di Francesco, J., Johnstone, D., Kirk, H., et al. 2008, *ApJS*, 175, 277
- Garden, R. P., Hayashi, M., Hasegawa, T., et al., 1991, *ApJ*, 374, 540
- Goldsmith, P. F., Snell, R. L., Hemeon-Heyer, M., et al. 1984, *ApJ*, 286, 599
- Henning, Th., Pfau, W., & Altenhoff, W. J., 1990, *A&A*, 227, 542
- Hughes, V. A., & Macleod, G. C. 1989, *A&A*, 97, 786
- Hosokawa, T., & Inutsuka, S. 2005, *ApJ*, 623, 917
- López-Sepulcre, A., Cesaroni, R. & Walmsley, C. M., 2010, *A&A*, 517, 66
- Menten, K. M., Pillai, T., & Wyrowski, F. 2005, *IAUS*, 227, 23
- Mercer, E. P., Clemens, D. P., Meade, M. R., et al. 2005, *ApJ*, 635, 560
- Paron, S., Cichowolski, S., & Ortega, M. E. 2009, *A&A*, 506, 789
- Paron, S., Petriella, A., & Ortega, M. E. 2011, *A&A*, 525, 132
- Pomarès, M., Zavagno, A., Deharveng, L., et al. 2009, *A&A*, 494, 987
- Qin, S. L., Wang, J. J., Zhao, G., Miller, M., & Zhao, J. H., 2008, *A&A*, 484, 361
- Rathborne, J. M., Jackson, J. M., & Simon, R. 2006, *ApJ*, 641, 389
- Robitaille, T. P., Marilynn, R. M., Babler, B. L., et al. 2008, *AJ*, 136, 2413
- Sherman, R. A. 2012, *ApJ*, 760, 58
- Simon, R., Jackson, J. M., Clemens, D. P., et al. 2001, *ApJ*, 551, 747
- Tibbs, C. T., Paladini, R., Compiègne, M., et al. 2012, *ApJ*, 754, 94
- Tibbs, C. T., Paladini, R., Compiègne, M., et al. 2012, *ApJ*, 754, 94
- Zavagno, A., Deharveng, L., Comerón, F., et al. 2006, *A&A*, 446, 171
- Zavagno, A., Pomarès, M., Deharveng, L., et al. 2007, *A&A*, 472, 835
- Zhang, Q., Hunter, T. R., Brand, J., et al. 2005, *ApJ*, 625, 864